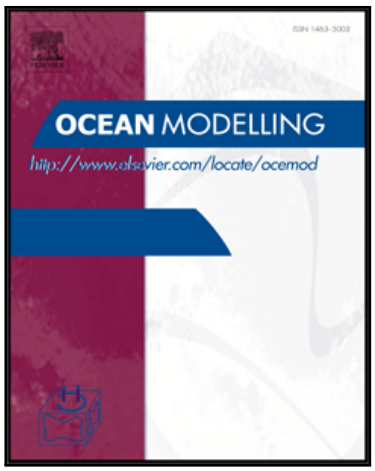

Southern Annular Mode impacts on global ocean surface waves

Andrew G. Marshall , Mark A. Hemer , Harry H. Hendon , Kathleen L. McInnes

PII: S1463-5003(18)30044-1
DOI: 10.1016/j.ocemod.2018.07.007
Reference: OCEMOD 1323

To appear in: *Ocean Modelling*

Received date: 15 February 2018
Revised date: 11 June 2018
Accepted date: 18 July 2018

Please cite this article as: Andrew G. Marshall , Mark A. Hemer , Harry H. Hendon , Kathleen L. McInnes , Southern Annular Mode impacts on global ocean surface waves, *Ocean Modelling* (2018), doi: 10.1016/j.ocemod.2018.07.007

Highlights

- **Statistically significant wave anomalies in the Southern Hemisphere covary with SAM surface zonal winds**
- **Significant wave anomalies are also detected in the central North Pacific and North Atlantic oceans during DJF**
- **The northern extratropical wave signals occur in connection with SAM teleconnections, independent of ENSO**
- **The SAM also influences the occurrence of daily low and high wave conditions**

The SAM may be a source of sub-weekly to seasonal predictability of surface wave

Southern Annular Mode impacts on global ocean surface waves

Andrew G. Marshall[1]

Mark A. Hemer[2]

Harry H. Hendon[3]

Kathleen L. McInnes[4]

1. Bureau of Meteorology, Hobart, Tasmania, Australia

2. CSIRO Oceans and Atmosphere, Hobart, Tasmania, Australia

3. Bureau of Meteorology, Docklands, Victoria, Australia

4. CSIRO Oceans and Atmosphere, Aspendale, Victoria, Australia

Friday, 1 June 2018

Corresponding Author: **Andrew G. Marshall**

Bureau of Meteorology

Hobart, Tasmania, Australia

Andrew.Marshall@bom.gov.au

ABSTRACT

We assess the impact of the Southern Annular Mode (SAM) on global ocean wind waves using 30 years of wave data from a wave model hindcast that is forced with high resolution surface winds from the NCEP-CFSR reanalysis. Our primary focus is on the wave field and swell influence in the Southern Hemisphere, and we apply our analysis to each of the four temperate-zone seasons comprising March-May (MAM), June-August (JJA), September-November (SON), and December-February (DJF). Statistically significant anomalies in significant wave height (H_s), peak wave period (T_p) and zonal wave energy flux (C_gE) are found to covary with local variations in surface zonal wind induced by the low and high polarity phases of the SAM.

The signature of the SAM in ocean surface waves extends beyond local wind-generated forcing in the Southern Hemisphere extratropics to remote forcing in the Northern Hemisphere extratropics during DJF, with the associated atmospheric signal resembling a tropically-forced Rossby wave train. This has a significant impact on surface waves in the central North Pacific and North Atlantic oceans. The El Niño Southern Oscillation (ENSO) acts to weaken the link between the SAM and Northern Hemisphere winter climate, with the zonal wind / divergence anomalies amplifying over the tropical Pacific Ocean when we exclude El Niño and La Niña years from the analysis. This remote link to the SAM thus occurs independent of ENSO via SAM-driven changes to the tropical atmospheric circulation, suggesting that the SAM may provide a useful predictive signal for the Northern Hemisphere during DJF. The SAM also influences the occurrence of daily low (below the 5th percentile) and high (above the 95th percentile) wave conditions, emphasizing that the SAM may be a valuable source of predictable

wave variability from sub-weekly to seasonal timescales. Future work should explore wave data suitable for trend analysis, considering the positive trend in the SAM over recent decades.

1 Introduction

The Southern Annular Mode (SAM, e.g. Trenberth 1979, Rogers and van Loon 1982, Mo and White 1985), or Antarctic Oscillation (Thompson and Wallace 1998), plays a dominant role in the high- and mid-latitude climate of the Southern Hemisphere. As an intrinsic mode of atmospheric variability, the SAM arises through a positive feedback between zonal-mean wind anomalies and eddy momentum fluxes and has a characteristic time scale of about two weeks (Lorenz and Hartmann 2001). Fluctuations in the SAM result from anomalous baroclinic wave activity in the extratropical storm track in association with fluctuations of the westerly jet stream. In its high polarity phase, a poleward shifted jet stream is associated with enhanced baroclinic wave activity that propagates upward and equatorward, thus providing momentum fluxes that reinforce the zonal wind anomalies against surface drag and causing the wind anomalies to drift poleward with a largely zonally symmetric, equivalent barotropic structure (e.g. Gong and Wang 1999, Thompson and Wallace 2000). Subsequently the mid-latitude westerly wind belt shifts poleward, characterising the high index polarity, or positive phase, of the SAM. Conversely, an equatorward shift in the mid-latitude westerly winds and reduction of baroclinic wave activity in the storm track characterises the negative SAM phase (e.g. Fyfe 2003).

The SAM influences variations in Southern Hemisphere weather and climate, and drives variations in the circulation in the Southern Ocean, over a wide range of timescales from daily to seasonal. Specifically, impacts of the SAM on weekly and monthly rainfall variability and extremes have been reported over Australia (e.g. Hendon *et al.* 2007, Risbey *et al.* 2009, Marshall et al. 2012, Marshall et al. 2014), New Zealand (Renwick and Thompson 2006), South America (Silvestri and Vera 2003), South Africa (Reason and Rouault 2005), and in the Northern Hemisphere (Zheng et al. 2015, Liu et al. 2015). The SAM has been linked to Antarctic temperature variations (e.g. Thompson and Solomon 2002) and sea-ice distribution (e.g. Lefebvre et al. 2004, Hall and Visbeck 2002), Southern Ocean surface temperature (e.g. Watterson 2000, 2001) and biology (e.g. Lovenduski and Gruber 2005), via its wind-driven impact on surface heat fluxes and Ekman drift. The importance of understanding these relationships to the SAM is underscored by the recent shift in the SAM towards a more positive phase, which is shown to contribute to observed long-term trends over the Southern Hemisphere (e.g. Thompson and Wallace 2000, Kushner *et al.* 2001, Haylock *et al.* 2006).

The purpose of this paper is to extend studies of the impact of ocean and explore its impact on global ocean wind waves. The relationships between global ocean surface waves and large-scale atmospheric climate variability have previously been investigated (e.g. Kushnir et al. 1997; Wang and Swail 2001; Dodet et al. 2010; Hemer et al. 2010; Izaguirre et al. 2011; Bosserelle et al. 2011; Semedo et al. 2011; Fan et al. 2012; Stopa et al. 2013), including the impact of the Madden-Julian Oscillation (Marshall et al. 2015). Hemer et al. (2010) identified that the principal mode of inter-annual variability of the Southern Hemisphere wave variability was significantly related to the SAM, focussing on

the local wind-generated forcing in the Southern Hemisphere extra-tropics and the consequent implications for swell waves that propagated equatorward in the major oceans basins. Despite this relationship, detailed analysis of this relationship has not been undertaken. The SAM is a probable candidate for driving significant surface wave variations due to its large spatial scale (hemispheric) and temporal scale (up to a season). Further, with increasing evidence to suggest an influence of the SAM on the Northern Hemisphere climate (e.g. Nan and Li 2003, Wu et al. 2009, Sun 2010, Sun et al. 2010), the relationship between the SAM and Northern Hemisphere surface wind-wave fields should be considered. For example, Liu et al. (2015) proposes an ocean-atmosphere coupled bridge as a key process by which the SAM signal in September-November (SON) can transmit to the Northern Hemisphere in December-February (DJF). In this mechanism, near-surface heat in the Southern Ocean is redistributed by SAM-driven changes in surface zonal wind. The SST signal can then persist into DJF via the memory of SST and, upon its release into the atmosphere, modify the upward branch of the Hadley cell. The meridional circulation of the Northern Hemisphere is thus affected and an anomalous DJF climate signal emerges at the surface. An important aspect of this inter-hemispheric teleconnection to the SAM is its independence from ENSO (Liu et al. 2015). Other recent work has also reported an ENSO-independent relationship between the SAM and atmospheric variability in the tropics during DJF (Ding et al. 2014).

Documenting and understanding the modulation of global ocean surface waves by the SAM can help underpin development of subseasonal predictive capability of ocean surface waves, with practical benefits that include anticipating wave-induced coastal inundation. This understanding will also be of benefit to the long-term management of

coasts. Projected 21st Century changes to the SAM are sensitive to the rate of ozone recovery and to greenhouse gas emission scenarios. Under a low RCP2.6 emission scenario, ozone recovery are expected to dominate, giving a small equatorward jet shift. Greenhouse gas emissions are expected to dominate under a high RCP8.5 emission scenario, giving an ongoing poleward jet shift (Christensen et al. 2013). Climate driven variability of the surface wave field is being increasingly recognised as a significant influence on shoreline position/stability, particularly in the context of projected future sea-level rise (Hemer et al. 2013, Barnard et al. 2015) Whether a low or high GHG emission scenario plays out, changes to the SAM will likely shift the equilibrium wave field for parts of the global ocean, with potential consequent implications for coastal sediment budgets and shoreline stability.

We assess the impact of the SAM on surface waves using the global output from a high resolution hindcast of a surface wave model forced by surface winds from a 31-year reanalysis. A description of the global ocean wave hindcast and its suitability for our study, along with the compositing approach to extract the SAM signals, are provided in Section 2. The impacts of the SAM on surface waves are presented in Section 3, and a summary and conclusions are provided in Section 4 including implications for sub-weekly to seasonal prediction of global surface wave variations.

2 Surface Wave Hindcast and SAM compositing

2.1 Surface Wave Hindcast

The Centre for Australian Weather and Climate Research (CAWCR) wave hindcast dataset (Durrant et al. 2014) is a high resolution global product created using the WAVEWATCH III^{TM} model version 4.08 (Tolman 1991; Tolman 2014) with 10m winds and sea ice concentration prescribed from the recent Climate Forecast System Reanalysis (CFSR; Saha et al. 2010) for the period 1979-2010. Available hourly and at $0.3^o \times 0.3^o$ horizontal resolution, the CFSR data provides an unprecedented depiction of global surface winds with sufficient representation of small scale high amplitude variability. In lieu of continuous global records of ocean surface waves, the CAWCR wave hindcast provides global wave data at a spatial resolution of 0.4° and at an hourly temporal resolution. Good agreement is found globally for bias and root mean square error relative to available satellite altimeter and buoy observations. Detailed assessments of the quality of this wave hindcast is presented for the Australian region in Hemer et al. (2017) and globally, with focus on Southern Pacific Island region, in Durrant et al. (2013). A description of its improvements over previously used products is also summarised in Marshall et al. (2015).

Here we utilise significant wave height (H_s), peak period (T_p) and wave energy flux (C_gE) from the large number of gridded variables available. These three represent the most commonly observed wave variable (H_s), the length of the waves and thus indication of the source of waves (T_p, where locally generated wind-sea will have short wave periods and distally generated swell will have longer wave periods), and the power of the waves (C_gE, providing an indication of the potential force of the waves on coastal or offshore infrastructure). C_gE depends on H_s and the period T thus

$$C_gE = \rho.g^2.H_s^2.T / 64\pi$$

where ρ is the water density and g is the gravitational acceleration. We are interested in assessing impacts of the SAM on both the magnitude and direction of surface wave energy, so we express the C_gE scalar field as a vector quantity to resolve the directional response by using peak wave direction (D_p) for deriving zonal and meridional components of C_gE (where D_p is decomposed into vector components and the C_gE scalar quantity comprises the magnitude of the total vector). For all surface wave fields assessed in this study we calculate anomalies relative to the annual climatology.

We note that temporally-varying sea ice concentration leads to a temporally-varying mask around the ice edge in the CAWCR hindcast. To ease calculations, the grid points that are periodically masked have been removed from our analysis for each season. Consequently, we do not consider the SAM's influence on wave fields in regions where the SAM has an impact on sea ice extent (e.g. Lefebvre et al. 2004, Hall and Visbeck 2002) and vice versa (e.g. Raphael et al. 2011). As such, this affects only a small area and does not impede our detection of the SAM's impact otherwise.

There exist biases in the hindcast that can be attributed to errors in the forcing wind field (Durrant et al. 2013). For instance, a known inhomogeneity in CFSR winds (Chawla et al. 2013) results in an over-prediction of wave heights in mid-latitudes in the early part of the hindcast, a common problem shared by global wave hindcast datasets. This leads to spurious trends in the wave data (Durrant et al. 2014). However, while biases in the wind can directly impact the wave field output in some cases, in other situations wind biases can have compensating effects on errors in the wave model (Durrant et al. 2013). The

focus of this previous work is on time-averaged biases, and so the limitations discussed in these studies do not necessarily hinder our composite analysis of climate variability on the subseasonal timescale. For example, we find that trend removal has little impact on our results (not shown); rather, the spurious trends in the wave data documented by Durrant et al. (2014) will impact long term climate studies using this data. We therefore refrain from performing trend analysis on this dataset.

2.2 SAM compositing

We diagnose impacts of the SAM on global ocean surface waves by constructing an index of the SAM that captures the variability of mean sea level pressure (MSLP) around the mid-latitudes of the Southern Hemisphere (e.g. Gong and Wang 1999, Marshall 2003, Marshall et al. 2012) using CFSR data (i.e. from the same reanalysis dataset prescribed for the CAWCR wave hindcast). Daily SAM indices are obtained by projecting daily zonal-mean MSLP anomalies onto the leading empirical orthogonal function (EOF) of observed monthly-mean MSLP anomalies between 25°S and 75°S, after removing the seasonal cycle from the data and weighting each grid point by the square root of the cosine of latitude (e.g. Marshall et al. 2012). The daily SAM index is then normalised by the standard deviation of the monthly SAM index. The EOF analysis is conducted on the base period 1979 to 2009 and each EOF is based on the covariance matrix.

The high index polarity (positive phase) of the SAM occurs when the pressure anomaly is low on the pole and the midlatitude westerly jet is shifted poleward. Conversely the low index polarity (negative phase) of the SAM occurs when the pressure

anomaly is high on the pole and the midlatitude westerly jet is shifted equatorward. Positive and negative SAM phases are defined to occur when index values exceed one standard deviation (σ) about the mean (i.e. > 1σ and < -1σ respectively). To first order, the positive and negative phases exhibit approximate symmetry in their broad-scale atmospheric characteristics, including their opposite signed but otherwise similar impacts on Australian climate anomalies (Hendon et al. 2007) and extremes (Marshall et al. 2014). The seasonal meridional shift in the mean position of the subtropical ridge between DJF and JJA (June-August) (due to the progression of the Australian monsoon trough and poleward contraction of the extratropical westerly jet) influences the spatial characteristics of the SAM at mid-latitudes, so we perform our assessment using subsets of daily-mean data for each temperate-zone season: MAM (March-May), JJA, SON, and DJF.

3 Results

3.1 Ocean wave response

We show the climatological mean fields for surface zonal wind and H_s (Figure 1), and for T_p and C_gE (Figure 2), calculated for each season, to provide context for understanding the SAM-induced wave anomalies. Each variable is derived directly from WAVEWATCH-III output files, following definitions provided in Tolman (2014), with T_p determined as the inverse of the wave peak frequency, f_p. Key features of the mean surface zonal wind in the Southern Hemisphere are dominant westerlies at mid-high

latitudes poleward of about 25°S in JJA and 30°S in DJF, where the SAM has a strong signal (not shown poleward of 60°S due to the ice mask in the hindcast data). Mean trade easterlies prevail in the subtropics year-round, except over the Maritime Continent in DJF, and the northwest Australian shelf in SON and DJF, where the mean winds in these seasons are westerly. In the mean surface wave fields, H_s maximizes in the higher latitudes where surface westerly winds are strongest, T_p tends to increase to the east which indicates swell propagation from the west, and C_gE shows wave energy propagating from the extratropics to the tropics.

The following analyses present composites of pertinent fields of interest, stratified according to season and SAM phase. The number of days *n* for each season pertaining to positive and negative SAM phases is shown in Table 1. To calculate statistical significance of composite anomalies, we use a standard t-test (Student 1908), but reduce the number of degrees of freedom to account for autocorrelation of the SAM index. The effective sample size is $n_{eff} \cong n\frac{1-\rho}{1+\rho}$, where ρ is the lag 1 autocorrelation of the SAM index at daily timescales. (e.g., Wilks 2006), which produces results similar to calculating n_{eff} as the aggregated number of discrete SAM episodes. Accordingly, the sample size is effectively reduced by a factor of 0.7-0.8, as indicated in Table 1.

In order to facilitate interpretation of the wind wave response to the SAM we first provide composite MSLP anomalies (Figure 3) and zonal wind anomalies (Figure 4) to show the spatial structure of the SAM. In all seasons, negative MSLP anomalies occur at high latitudes and positive MSLP anomalies occur at mid-latitudes, with anomalous westerly flow centred near 60°S juxtaposed against anomalous easterly flow centred near 35°S. We note the meridional shift in the location of peak easterlies between JJA (~30-

35°S) and DJF (~35-40°S) consistent with the seasonal migration of the subtropical ridge. We also note a clear link to the Northern Hemisphere extratropics in DJF when a weak but significant north-south dipole anomaly appears in the central North Pacific comprising westerlies to the north and easterlies to the south during the positive SAM phase, and roughly the opposite during the negative SAM phase. This indicates an anomalous anticyclone (during positive SAM) and cyclone (during negative SAM) in the central North Pacific (not shown here in the southern hemispheric projections of Figure 3, but seen later in the global analysis of Figure 8). There also appears a hint of a signal in the North Atlantic Ocean comprising easterlies centred on 60°N and westerlies centred on 40°N during the positive SAM phase in DJF, indicating cyclonic flow. (Only the westerly signal appears significant; the easterly anomaly is seen contoured with a magnitude of -1 ms^{-1} near 320-330°E.) Together these patterns resemble a Rossby wave train emanating away from the tropics into the winter hemisphere, such as occurs in response to tropical forcing associated with SST anomalies (e.g. Trenberth et al. 1998). In addition, previous studies have shown the SAM to be anticorrelated with ENSO in DJF, such that a positive SAM is often associated with La Niña and a negative SAM is often associated with El Niño (e.g. Zhou and Yu 2004, Carvalho et al. 2005, Ding et al. 2012). It therefore stands to reason that ENSO could be at the heart of this inter-hemispheric high-latitude teleconnection via (i) its relationship to the SAM and (ii) its role as a tropical heating source for Rossby wave propagation into the Northern Hemisphere. However, in Section 3.3 we show this teleconnection to be independent of ENSO, consistent with recent work (e.g. Liu et al. 2015), and that ENSO rather acts to dampen the Northern Hemispheric response.

The composite evolution of the global response of ocean surface waves to the SAM is explored for H_s anomalies in Figure 5, T_p anomalies in Figure 6, and zonal C_gE anomalies in Figure 7, with shading applied for statistically significant anomalies to 95% confidence. Interpretation of the SAM wave anomalies is aided by referencing the zonal wind anomalies (Figure 4) and the mean wind and wave fields (Figures 1 and 2). In general, H_s anomalies are largest over the Southern Hemisphere extratropics concomitant with the strong zonal wind signature of the SAM. Here, positive H_s anomalies occur where SAM westerly anomalies act on mean state westerly winds; in a high latitude zonal band during the positive SAM phase (up to around 1 m), and in mid-latitude nodes centred near 40°S during the negative SAM phase (up to 0.6 m). Conversely, negative H_s anomalies of similar magnitude occur concurrently with easterly anomalies in these regions, i.e. at high latitudes during the negative SAM phase and at mid-latitudes during the positive SAM phase. A notable feature is the protrusion of the high-latitude wind anomaly into the mid-latitudes around 250°E, and the resulting equatorward expansion of positive H_s anomalies during the positive SAM phase (and negative H_s anomalies during the negative SAM phase) again amplified where the SAM wind anomalies act on a strong mean state. The Northern Hemisphere extratropical wind features are also reflected in the H_s field, with anomalies of up to 0.3-0.4 m occurring in the central North Pacific and North Atlantic oceans in DJF; these appear statistically significant for the negative phase of the SAM.

T_p anomalies in Figure 6 demonstrate the broad-scale impact of the SAM in directly forcing surface waves primarily in the mid-high latitudes of the Southern Hemisphere. T_p anomalies are statistically significant and strongest across the Southern and South Pacific

oceans concurrent with the large anomalies in zonal C_gE. The increase in T_p towards the eastern Pacific, and the in-phase variation of T_p with H_s, suggest that the anomalous wave growth in the positive SAM phase (increased T_p) and reduction in the negative SAM phase (decreased T_p) is primarily generated by ocean swell. The annular characteristic of the SAM influences the strength of T_p anomalies, whereby large positive / negative T_p anomalies relate to the large zonal breadth of westerlies / easterlies. Similar responses occur in the tropical Pacific and Indian oceans, and in the North Atlantic during DJF (although less pronounced for these remote regions), with the in-phase associations between T_p and H_s again being indicative of swell signals. In some scarce regions, however, such as east of New Zealand year-round and south of Alaska during JJA, local wave generation dominates and thus the T_p and H_s signals appear out of phase. (The region to the east of New Zealand is sheltered from the influence of Southern Ocean swell, and to the south of Alaska local wave generation is high with little to no swell contribution.) Note also the strong significant signal in T_p on the northwest Australian shelf, which we consider in the following section with a closer look at the SAM-wave response around the Australian coastline.

Zonal C_gE anomalies in Figure 7 also broadly reflect the SAM zonal wind signal, with positive values indicating wave energy anomalies emanating from the west (towards the east) and negative values indicating wave energy anomalies emanating from the east (towards the west). As previously stated, the climatological mean fields for CgE (Figure 2) show wave energy propagating with a meridional component, from the extra-tropics to the tropics, as swell propagates along the great circle paths. Thus, these zonal anomalies

should be interpreted as not only a change in magnitude of CgE, but also a rotation in direction of the wave energy flux.

3.2 Australian coastal wave response

Significant wave responses to the SAM occur around the Australian coastline year-round, varying in their spatial extent from season to season. During the positive SAM phase, negative H_s anomalies of amplitude 0.1-0.2 m are seen along the northwest Australian shelf primarily during SON and DJF. Similar magnitude negative anomalies of H_s are also seen off the southwest Australian coast in all seasons (Figure 5). In JJA, these negative anomalies extend halfway along the Western Australian coastline: these coastal impacts are approximately equal and opposite during the negative SAM phase, and thus the SAM induces a strong and significant impact on wave height in the vicinity of the Leeuwin Current (± 0.3-0.4 m) during its peak flow in JJA (Smith et al. 1991; Pearce 1997). These impacts are associated with (i) easterly wind anomalies during the positive SAM phase, and (ii) westerly wind anomalies during the negative SAM phase (Figure 3), acting on a westerly mean state (Figure 1).

For the east coast of Australia, the greatest impacts on H_s occur during DJF and JJA, again with amplitudes around ± 0.1-0.2 m. For DJF, the response appears somewhat non-linear; the positive SAM phase sees a weak increase in H_s that hugs the south-eastern coastline from around Brisbane (27°S, 153°E) to Tasmania. This is seemingly a response to anti-clockwise rotation of the south-westerly wave fluxes (Figure 6), resulting in a greater contribution of swell energy propagating into the Tasman Sea. During the

negative SAM phase a decrease in H_s is seen further to the north along the Queensland east coast. The SAM impact on H_s during JJA shows an increase along the Queensland and Northern Territory coastlines between the Tropic of Capricorn (23.5°S) and Darwin (12°S, 131°E) during the positive SAM phase, and a decrease along the Great Barrier Reef during the negative SAM phase. These impacts are associated with (i) easterly wind anomalies during the positive SAM phase, and (ii) westerly wind anomalies during the negative SAM phase, acting on an easterly mean state.

The strongest impact on Australian coastal T_p anomalies in Figure 6 appears on the northwest Australian shelf with amplitudes up to around 2 s. Importantly, these values are about half of the climatological mean (Figure 2), and thus highlight a strong shadow zone that suggests a directional shift in the Southern Ocean generated swell component of the wave field. North West Cape on the northwest shelf separates two distinct wave regimes, owing to the change in influence of swell generated in the Southern Ocean versus waves generated in the eastern tropical Indian Ocean (Greenslade et al., 2018). Here, the swell observed on the northwest shelf is generated in the Indian Ocean extra-tropics, which propagates north-eastwards to the shelf. During the positive phase of the SAM, the wave energy flux is rotated anti-clockwise, and energy which would have propagated onto the northwest shelf is now blocked by North West Cape. Consequently, the wave regime north of the Cape is sensitive to the phase of the SAM (positive SAM is associated with lower Hs, Tp and CgE in almost all seasons). Elsewhere around the Australian coast, the strongest impacts on anomalous T_p are found around Tasmania and the southeast in most seasons, extending up from the Southern Ocean. In this region, a protrusion of H_s anomalies occurs from higher latitudes during MAM and JJA. This is particularly seen

around Tasmania in both seasons and into the Great Australian Bight in MAM, such that they are of opposite sign to those in SON and DJF which are sourced from the mid-latitudes. This is also the case for zonal C_gE anomalies in Figure 7. Otherwise, wave energy flux anomalies around the Australian coastline are from the east during the positive SAM phase (a general anti-clockwise rotation of the south-westerly CgE vectors), and from the west during the negative SAM phase (a clockwise rotation), in line with the orientation of zonal wind anomalies around the continent.

3.3 ENSO influence

The positive SAM phase is significantly correlated with the cool phase of the El Niño - Southern Oscillation (ENSO) in DJF using data on timescales from daily (Marshall et al. 2012) to seasonal (L'Heureux and Thompson 2006, Hendon et al. 2007). We therefore consider the possible impact of ENSO on our results by repeating the MSLP, zonal wind and wave field calculations of Figures 3-7 for DJF, but excluding El Niño and La Niña episodes, in order to isolate the impact of the SAM during neutral ENSO years. This reduces the DJF sample sizes by a factor of about a half for the positive SAM phase and two thirds for the negative SAM phase (Table 1). We note that we also repeated the analyses for the other seasons with ENSO years excluded but there was little change to our results (not shown).

Global MSLP composite anomalies in Figure 8 highlight the northern hemispheric link to the SAM with the emergence of an anticyclone over the central North Pacific and a cyclone over the North Atlantic Ocean during the positive SAM which weakens

considerably with the inclusion of ENSO years (not shown). A signal of comparable strength and opposite sign occurs over the central North Pacific during the negative SAM phase. Composite anomalies for 10m zonal wind, H_s, T_p and C_gE in Figure 8 also show a strong intensification of the Northern Hemisphere extratropical signal, compared with when ENSO years are included (Figures 4-7), particularly over the North Atlantic Ocean during the positive SAM phase. (Only the positive wave field anomalies centred near 30°N during the negative SAM phase are similar in strength, but the region of significance is reduced, when ENSO years are excluded.) This indicates that El Niño and La Niña play a key role in offsetting this signal. Indeed, the 10m zonal wind composite of Figure 8 (strong SAM without ENSO years) indicates a region of strong divergence anomalies over the equatorial western-central Pacific that appears relatively weak in Figure 4 (strong SAM with ENSO years), and thus the SAM shows a clear link to variations in the atmospheric circulation of the tropics that are independent of ENSO. This signal is consistent with the role of upper-level tropical divergence in driving these tropical-extratropical teleconnections via the Hadley Cell (e.g. Hoskins and Karoly 1981). The impact on zonal wind here is reflected in the H_s field, with statistically significant anomalies of up to 0.8 m occurring in the North Atlantic, and up to 0.6 m in the central North Pacific, during neutral ENSO years when the SAM is positive. These signals are about twice the strength of those seen when ENSO years are included. Moreover, the remote North Atlantic signal is of comparable strength to the directly forced signal in the Southern Hemisphere, courtesy of the large amplitude westerly wind anomalies (Figure 4) that act on a strong westerly mean state (Figure 1).

The other wave fields show similar amplifications of the Northern Hemisphere signal in DJF during neutral ENSO years. Peak period anomalies occur with amplitudes up to about 0.8 s in the North Atlantic and central North Pacific (c.f. 0.4 s in Figure 7). Wave energy flux anomalies occur up to 50 kW m^{-1} in the North Atlantic (c.f. 30 kW m^{-1} in Figure 6) and 30 kW m^{-1} in the central North Pacific (c.f. 25 kW m^{-1}), the former of which represents about half of the mean amplitude (Figure 2). These remotely forced signals point to a significant and stronger teleconnection between the SAM and Northern Hemisphere winter climate during neutral ENSO years, compared with active ENSO years. Consistent with recent work that also reports an ENSO-independent link between the SAM and Northern Hemisphere extratropical climate (Liu et al. 2015), this result deserves further investigation beyond the scope of the present study.

3.4 Shifts in low and high wave conditions

We now explore how the SAM acts to modulate the tails of the distribution of H_s, i.e. how the SAM acts to cause shifts in occurrence of low and high wave conditions. Low wave conditions are defined as occurring when H_s anomalies are below the 5^{th} percentile, and high wave conditions when H_s anomalies are above the 95^{th} percentile. Figure 9 shows the 5^{th} (left column) and 95^{th} (right column) percentile thresholds (relative to the mean H_s shown in Figure 1) to vary mostly in latitude, with zonal uniformity over the globe and the largest excursions in the extratropics. These spatial patterns reflect the variance in H_s occurring strongest at mid-high latitudes (not shown) where the mean H_s is highest. Outside of the tropics the 95^{th} percentile threshold anomaly is about 0.5 m

stronger than the 5th percentile thresholds, which stems from the strongly positively skewed distribution of H_s (not shown). In the tropics the high and low thresholds are similar, indicating that H_s is more normally distributed at lower mean wind speeds.

Based on these 5th and 95th percentile thresholds, we compute the probability of occurrence of low and high wave conditions for positive and negative SAM phases by counting the number of instances at each grid location for which the H_s anomaly is (i) less than the 5th percentile threshold and (ii) greater than the 95th percentile threshold, and then dividing by the total number of samples in each SAM phase. In Figures 10 (for the 5th percentile) and 11 (for the 95th percentile) we express probability composites as ratios relative to the mean probability of occurrence (nominally 0.05); probability ratios greater than one indicates an increased likelihood of low wave conditions in Figure 10 and high wave conditions in Figure 11. Conversely, probabilities less than one indicate decreased likelihood of occurrence. Ratios are shaded only when significantly different from one at 95% confidence using a z-score test for event probabilities (Spiegel 1961).

Probabilities of low and high wave conditions are broadly consistent with the spatial variations in H_s anomalies seen in Figure 5. In general, significant decreases in the likelihood of low wave conditions (Figure 10) and increases in the likelihood of high wave conditions (Figure 11) occur at high latitudes during the positive SAM phase, and at mid-latitudes during the negative SAM phase, in conjunction with regions of positive H_s anomalies (Figure 5). Conversely, significant increases in the likelihood of low wave conditions and decreases in the likelihood of high wave conditions generally occur at mid-latitudes during the positive SAM phase, and at high latitudes during the negative SAM phase, in conjunction with negative H_s anomalies (Figure 5). (Note that high ratios

in Figure 10 and low ratios in Figure 11 use blue shading, whereas low ratios in Figure 10 and high ratios in Figure 11 use orange shading, for easy comparison with negative blue and positive orange shading of anomalies in Figure 5.) Notably, with Australian coastal impacts in mind, the increase in the probability of high wave conditions during the negative SAM phase (Figure 11) is up to twice the mean probability of occurrence in association with the anomalies in westerly wind (Figure 4) and positive H_s (Figure 5). Furthermore, the SAM teleconnections to the central North Pacific and North Atlantic Ocean also occur here, again concurrent with H_s anomalies. These teleconnections are again enhanced in DJF when ENSO years are excluded from the analysis (not shown). We also note with interest the high probability of low wave conditions that spans the western coast of South America during the negative SAM phase in DJF and MAM, and the high probability of low wave conditions along the Indonesian coast during the positive SAM phase (Figure 10). Considering the positive trend in the SAM over recent decades (e.g. Marshall 2003), the latter may suggest declining wave conditions along the Indonesian surf coast. In general the probability ratios for low wave conditions are stronger than for high wave conditions, reflecting the slightly weaker (negative) thresholds for low wave occurrence (1.5-2.0 m at mid-latitudes), compared with high wave occurrence (2.0-2.5 m).

4 Summary and concluding remarks

This paper assesses the impact of the SAM on global ocean wind waves during each of the four temperate-zone seasons using 30 years of high-resolution wave data from the

CAWCR wave hindcast. Anomalies in H_s, T_p and C_gE show a strong and significant response over the Southern Hemisphere extratropics year-round, concomitant with the strong zonal wind signature of the SAM. In regions dominated by mean westerlies, increases in H_s of up to 1 m occur concurrently with westerly anomalies, while negative H_s anomalies of similar magnitude occur concurrently with easterly anomalies. Wave impacts occur around the Australian coast at various times of year with amplitudes of 0.3-0.4 m off the southwest coast year-round, 0.1-0.2 m on the northwest Australian shelf in SON and DJF, and 0.1-0.2 m along the east coast in JJA and DJF. The Tasmanian coast experiences wave impacts primarily from higher latitudes in MAM and JJA, which extend also into the Great Australian Bight in MAM. T_p and zonal C_gE anomalies broadly reflect the SAM zonal wind signal in directly forcing surface waves primarily in the mid-high latitudes of the Southern Hemisphere. Moreover, the increase in T_p towards the eastern Pacific, and the in-phase variation of T_p with H_s, suggest the wave anomalies are primarily generated by an increase in contribution from the swell component of the wave spectrum. The strength of T_p anomalies varies with the zonal wind fetch over the Southern Ocean, and the strongest impact on T_p anomalies around the Australian coast is on the northwest shelf with amplitudes up to around 2 s, approximately half of the climatological mean.

Surface wind and wave variables offer a useful climate diagnostic for resolving a remote teleconnection to the Northern Hemisphere extratropics in DJF when an atmospheric signal emerges resembling a tropically-forced Rossby wave train. This has a significant impact on surface waves in the central North Pacific and North Atlantic oceans, where anomalies of up to 0.3-0.4 m (around 5-10% of the mean amplitude) occur

for H_s, 0.4 s (about 5% of the mean amplitude) for T_p, and 30 kW m^{-1} (about 30% of the mean amplitude) for zonal C_gE. The zonal wind patterns suggest anticyclonic/cyclonic responses over the central North Pacific Ocean (anticyclonic during positive SAM) and North Atlantic Ocean (cyclonic during positive SAM). These remote signals amplify significantly when we exclude El Niño and La Niña years from the analysis, indicating that ENSO plays a key role in offsetting the link between the SAM and Northern Hemisphere winter climate. This appears to be related to a weakening of zonal wind / divergence anomalies over the tropical Pacific Ocean when the SAM is strong during active ENSO years. Importantly, this remote link to the SAM occurs independent of ENSO via changes to the tropical atmospheric circulation / Hadley Cell, consistent with recent studies.

The SAM also imposes a strong and significant influence on the occurrence of low and high wave conditions, defined when H_s anomalies are below the 5th percentile and above the 95th percentile respectively. In general, significant increases in the likelihood of high wave conditions and decreases in the likelihood of low wave conditions correspond to regions where the SAM induces positive H_s anomalies. Notably, a two-fold increase in the probability of high wave conditions occurs in the Australian region. Again, the impact of the SAM extends to the central North Pacific and North Atlantic Ocean concurrent with H_s anomalies.

The modulation of surface wave activity by the SAM presented here supports the results of a similar analysis for the Madden-Julian Oscillation by Marshall et al. (2015) in suggesting potential predictability of global wave variations on the subseasonal timescale, which could have tremendous practical benefit. Good progress has been made in

improving the depiction of the SAM in global forecast models and predictability of the SAM has been demonstrated out to lead times approaching three weeks (e.g. Marshall et al. 2012). Climatologically driven changes in the wave climate are increasingly being recognised as a key influence on coastal erosion and accretion patterns, and consequent shoreline position for the world's coasts (e.g. Barnard et al. 2015). Similarly, coastal engineers are beginning to consider pre-emptive coastal management options to limit damage to storm wave events (Davidson et al. 2017). Subseasonal predictability of surface wave variations associated with the SAM (and other climate drivers) has the potential to provide coastal managers with sufficient and timely information that could enable them to make decisions that could protect or limit coastal communities and infrastructure from severe wave damage. Thus subseasonal predictability of surface wave variations resulting from the SAM should now be investigated.

Acknowledgements. This study was supported through funding from the Earth System and Climate Change Hub of the Australian Government's National Environmental Science Programme, as part of the Coastal Hazards Project 2.10. Our global ocean surface wave data was generated as part of the Pacific-Australia Climate Change Science and Adaptation Planning (PACCSAP) program. We thank Dr Tom Durrant for work on a previous manuscript using this data, and the anonymous journal reviewers for providing helpful comments and suggestions.

REFERENCES

Barnard, P.L., Short, A.D., Harley, M.D., Splinter, K.D., Vitousek, S., Turner, I.L., Allan, J., Banno, M., Bryan, K.R., Doria, A., Hansen, J.E., Kato, S., Kuriyama, Y., Randall-Goodwin, E., Ruggiero, P., Walker, I.J., Heathfield, D.K., 2015. Coastal vulnerability across the Pacific dominated by El Niño/Southern Oscillation. Nature Geoscience 8, 801-807.

Bosserelle, C., Pattiaratchi, C., Haigh, I., 2011. Inter-annual variability and longer-term changes in the wave climate of Western Australia between 1970 and 2009. Ocean Dynamics 62 (1), 63-76.

Carvalho, L. M. V., Jones, C., Ambrizzi, T., 2005. Opposite phases of the Antarctic Oscillation and relationships with intraseasonal to interannual activity in the tropics during the austral summer. Journal of Climate 18, 702-718.

Chawla, A., Spindler, D.M., Tolman, H.L., 2013. Validation of a thirty year wave hindcast using the Climate Forecast System Reanalysis winds. Ocean Modelling 70, 189-206.

Christensen, J.H., Kumar, K.K., Aldrian, E., An, S.-I., Cavalcanti, I.F.A., de Castro, M., Dong, W., Goswami, P., Hall, A., Kanyanga, J.K., Kitoh, A., Kossin, J., Lau, N.-C., Renwick, J., Stephenson, D.B., Xie, S.-P., Zhou, T., 2013. Climate Phenomena and their Relevance for Future Regional Climate Change. In: Climate Change 2013: The Physical Science Basis. Contribution of Working Group I to the Fifth Assessment Report of the

Intergovernmental Panel on Climate Change [Stocker, T.F., Qin, D., Plattner, G.-K., Tignor, M., Allen, S.K., Boschung, J., Nauels, A., Xia, Y., Bex, V., Midgley, P.M. (eds.)]. Cambridge University Press, Cambridge, United Kingdom and New York, NY, US.

Davidson, M.A., Turner, I.L., Splinter, K.D., Harley, M.D., 2017. Annual prediction of shoreline erosion and subsequent recovery. Coastal Engineering 130, 14-25.

Ding, Q., Steig, E.J., Battisti, D.S., Wallace, J.M., 2012. Influence of the tropics on the Southern Annular Mode. Journal of Climate 25, 6330-6348.

Ding, H., Greatbatch, R.J., Gollan, G., 2014. Tropical influence independent of ENSO on the austral summer Southern Annular Mode. Geophys. Res. Lett. 41, 3643-3648.

Dodet, G., Bertin, X., Taborda, R., 2010. Wave climate variability in the North-East Atlantic Ocean over the last six decades. Ocean Modelling 31 (3-4), 120-131.

Durrant, T.H., Greenslade, D.J.M., Simmonds, I., 2013. The effect of statistical wind corrections on global wave forecasts. Ocean Modelling 70, 116-131.

Durrant, T., Greenslade, D., Hemer, M., Trenham, C., 2014. A Global Wave Hindcast focussed on the Central and South Pacific. CAWCR Technical Report 070.

Fan, Y., Lin, S.-J., Held, I.M., Yu, Z., Tolman, H.L., 2012. Global ocean surface wave simulation using a coupled atmosphere-wave model. Journal of Climate 25 (18), 6233-6252.

Fyfe, J.C., 2003. Separating extratropical zonal wind variability and mean change. Journal of Climate 16, 863-874.

Gong, D., Wang, S., 1999. Definition of Antarctic Oscillation index. Geophysical Research Letters 26, 459-462.

Greenslade, D., Zanca, A., Zieger S., Hemer, M., 2018. Optimising the Australian Wave Observation Network. Journal of Southern Hemisphere Earth Systems Science, submitted.

Hall, A., Visbeck, M., 2002. Synchronous variability in the Southern Hemisphere atmosphere, sea ice, and ocean resulting from the Annular Mode. Journal of Climate 15, 3043-3057.

Haylock, M.R., Peterson, T.C., Alves, L.M., Ambrizzi, T., Anunciacao, Y.M.T., Baez, J., Barros, V.R., Berlato, M.A., Bidegain, M., Coronel, G., Corradi, V., Garcia, V.J., Grimm, A.M., Karoly, D., Marengo, J.A., Marino, M.B., Moncunill, D.F., Nechet, D., Quintana, J., Rebello, E., Rusticucci, M., Santos, J.L., Trebejo, I., Vincent, L.A., 2006. Trends in

total and extreme South American rainfall in 1960–2000 and links with sea surface temperature. Journal of Climate 19, 1490-1512.

Hemer, M.A., Church, J.A., Hunter, J.R., 2010. Variability and trends in the directional wave climate of the Southern Hemisphere. International Journal of Climatology 30 (4), 475-491.

Hemer, M., Yalin, F., Nobuhito, M., Alvaro, S., Wang, X., 2013. Projected changes in wind climate from a multi-model ensemble. Nature Climate Change 3, 471-476.

Hemer, M.A., Zieger, S., Durrant, T., O'Grady, J., Hoeke, R.K., McInnes, K.L., Rosebrock, U., 2017. A revised assessment of Australia's national wave energy resource. Renewable Energy 114(A), 85-107.

Hendon, H.H., Thompson, D.W.J., Wheeler, M.C., 2007. Australian Rainfall and Surface Temperature Variations Associated with the Southern Hemisphere Annular Mode. Journal of Climate 20, 2452-2467.

Hoskins, B.J., Karoly, D.J., 1981. The steady linear response of a spherical atmosphere to thermal and orographic forcing. Journal of Atmospheric Science 38, 1179-1196.

Izaguirre, C., Méndez, F.J., Menéndez, M., Losada, I.J., 2011. Global extreme wave height variability based on satellite data. Geophysical Research Letters 38, L10607.

Kushner, P.J., Held, I.M., Delworth, T.L., 2001. Southern Hemisphere atmospheric circulation response to global warming. Journal of Climate 14, 2238-2249.

Kushnir, Y., Cardone, V.J., Greenwood, J.G., Cane, M., 1997. On the recent increase in North Atlantic wave heights. Journal of Climate 10, 2107-2113.

Lefebvre, W., Goosse, H., Timmermann, R., Fichefet, T., 2004. Influence of the southern annular mode on the sea ice–ocean system. Journal of Geophysical Research 109, C09005, doi:10.1029/2004JC002403.

L'Heureux, M.L., Thompson, D.W.J., 2006. Observed relationships between the El Niño-Southern Oscillation and the extratropical zonal-mean circulation. Journal of Climate 19, 276-287.

Liu, T., Li, J., Zheng, F., 2015. Influence of the boreal autumn southern annular mode on winter precipitation over land in the Northern Hemisphere. Journal of Climate 28, 8825-8839.

Lorenz, D.J., Hartmann, D.L., 2001. Eddy-zonal flow feedback in the Southern Hemisphere. Journal of Atmospheric Science 58, 3312-3327.

Lovenduski, N.S., Gruber, N., 2005. Impact of the Southern Annular Mode on Southern Ocean circulation and biology. Geophysical Research Letters 32, L11603.

Marshall, G.J., 2003. Trends in the Southern Annular Mode from observations and reanalyses. Journal of Climate 16, 4134-4143.

Marshall, A.G., Hudson, D., Wheeler, M.C., Hendon, H.H., Alves, O., 2012. Simulation and prediction of the Southern Annular Mode and its influence on Australian intra-seasonal climate in POAMA. Climate Dynamics 38, 2483-2502.

Marshall, A.G., Hudson, D., Wheeler, M.C., Alves, O., Hendon, H.H., Pook, M.J., Risbey, J.S., 2014. Intra-seasonal drivers of extreme heat over Australia in observations and POAMA-2. Climate Dynamics 43, 1915-1937.

Marshall, A.G., Hendon, H.H., Durrant, T.H., Hemer, M.A., 2015. Madden Julian Oscillation impacts on global ocean surface waves. Ocean Modelling 96, 136-147.

Mo, K.C., White, G.H., 1985. Teleconnections in the Southern Hemisphere. Mon Weather Rev 113, 22-37.

Nan, S., Li, J., 2003. The relationship between the summer precipitation in the Yangtze River valley and the boreal spring Southern Hemisphere annular mode. Geophysical Research Letters 30, 2266.

Pearce, A.F., 1997. "The Leeuwin Current and the Houtman Abrolhos Islands, Western Australia", In Wells, F. E.., The Marine Flora and Fauna of the Houtman Abrolhos Islands, Western Australia, Volume 1, Perth: Western Australian Museum, pp. 11-46.

Raphael, M.N., Hobbs, W., Wainer, I., 2011. The effect of Antarctic sea ice on the Southern Hemisphere atmosphere during the southern summer. Climate Dynamics 36, 1403-1417.

Reason, C.J.C., Rouault, M., 2005. Links between Antarctic Oscillation and winter rainfall over western South Africa. Geophysical Research Letters 32, L07705, doi:10.1029/2005GL022419.

Renwick, J., Thompson, D.W.J., 2006. The Southern Annular Mode and New Zealand climate. Water & Atmosphere 14, 24-25.

Risbey, J.S., Pook, M.J., McIntosh, P.C., Wheeler, M.C., Hendon, H.H., 2009. On the Remote Drivers of Rainfall Variability in Australia. Monthly Weather Review 137, 3233-3253.

Rogers, J.C., van Loon, H., 1982. Spatial variability of sea level pressure and 500 mb height anomalies over the Southern Hemisphere. Monthly Weather Review 110, 1375-1392.

Saha, S., Moorthi, S., Pan, H.-L., Wu, X., Wang, J., Nadiga, S., Tripp, P., Kistler, R., Woollen, J., Behringer, D., Liu, H., Stokes, D., Grumbine, R., Gayno, G., Wang, J., Hou, Y.-T., Chuang, H.-Y., Juang, H.-M.H., Sela, J., Iredell, M., Treadon, R., Kleist, D., Van Delst, P., Keyser, D., Derber, J., Ek, M., Meng, J., Wei, H., Yang, R., Lord, S., Van Den Dool, H., Kumar, A., Wang, W., Long, C., Chelliah, M., Xue, Y., Huang, B., Schemm, J.-K., Ebisuzaki, W., Lin, R., Xie, P., Chen, M., Zhou, S., Higgins, W., Zou, C.-Z., Liu, Q., Chen, Y., Han, Y., Cucurull, L., Reynolds, R.W., Rutledge, G., Goldberg, M., 2010. The NCEP Climate Forecast System Reanalysis. Bulletin of the American Meteorological Society 91, 1015-1057.

Semedo, A., Suselij, K., Rutgersson, A., Sterl, A., 2011. A global view on the wind sea and swell climate and variability from ERA-40. Journal of Climate 24 (5), 1461-1479.

Silvestri, G.E., Vera, C.S., 2003. Antarctic Oscillation signal on precipitation anomalies over southeastern South America. Geophysical Research Letters 30, 2115, doi:10.1029/2003GL018277.

Smith, R.L., Huyer, A., Godfrey, J.S., Church, J., 1991. The Leeuwin Current off Western Australia, 1986–1987. Journal of Physical Oceanography 21, 323-345.

Spiegel, M.R., 1961. Schaum's outline of theory and problems of statistics. Schaum Publishing Company, New York, 359 pp.

Stopa, J.E., Cheung, K.-F., Tolman, H.L., Chawla, A., 2013. Patterns and cycles in the climate forecast system reanalysis wind and wave data. Ocean Modelling 70, 207-220.

Student, 1908. The probable error of a mean. Biometrika 6, 1-25.

Sun, J., 2010. Possible impact of the boreal spring Antarctic Oscillation on the North American summer monsoon. Atmospheric and Oceanic Science Letters 3, 232-236.

Sun, J., Wang, H., Yuan, W., 2010. Linkage of the boreal spring Antarctic Oscillation to the West African summer monsoon. Journal of the Meteorological Society of Japan 88, 15-28.

Thompson, D.W.J., Wallace, J.M., 1998. The Arctic Oscillation signature in the wintertime geopotential height and temperature fields. Geophysical Research Letters 25, 1297-1300.

Thompson, D.W.J., Wallace, J.M., 2000. Annular Modes in the Extratropical Circulation. Part I: Month-to-Month Variability. Journal of Climate 13, 1000-1016.

Thompson, D.W.J., Solomon, S., 2002. Interpretation of recent Southern Hemisphere climate change. Science 296, 895-899.

Tolman, H.L., 1991. A Third-Generation Model for Wind Waves on Slowly Varying, Unsteady, and Inhomogeneous Depths and Currents. Journal of Physical Oceanography, 21 (6), 782-797.

Tolman, H.L., 2014. User manual and system documentation of WAVEWATCH III™ version 4.18. Technical Note 316, NOAA/NWS/NCEP/MMAB.

Trenberth, K.E., 1979. Interannual variability of the 500 mb zonal-mean flow in the Southern Hemisphere. Monthly Weather Review 107, 1515-1524.

Trenberth, K. E., Branstator, G. W., Karoly, D., Kumar, A., Lau, N-C., Ropelewski, C., 1998. Progress during TOGA in understanding and modeling global teleconnections associated with tropical sea surface temperatures. Journal of Geophysical Research 103, 14291-14324.

Wang, X.L., Swail, V.R., 2001. Changes of extreme wave heights in Northern Hemisphere Oceans and related atmospheric circulation regimes. Journal of Climate 14 (10), 2204-2221.

Watterson, I.G., 2000. Southern midlatitude zonal wind vacillation and its interaction with the ocean in GCM simulations. Journal of Climate 13, 562-578.

Watterson, I.G., 2001. Zonal wind vacillation and its interaction with the ocean: implications for interannual variability and predictability. Journal of Geophysical Research 106, 23965-23975.

Wilks, D. S., 2006. Statistical Methods in the Atmospheric Sciences. Academic Press, 648 pp.

Wu, Z.W., He, J.H., Wang, B., Liu, X., 2009. Can the Southern Hemisphere annular mode affect China winter monsoon? Journal of Geophysical Research 114, D11107.

Zheng, F., Li, J.P., Wang, L., Xie, F., Li, X., 2015. Cross-seasonal influence of the December–February Southern Hemisphere annular mode on March–May meridional circulation and precipitation. Journal of Climate 28, 6859-6881.

Zhou, T., Yu, R., 2004. Sea-surface temperature induced variability of the Southern Annular Mode in an atmospheric general circulation model. Geophysical Research Letters 31, L24206.

Figure captions

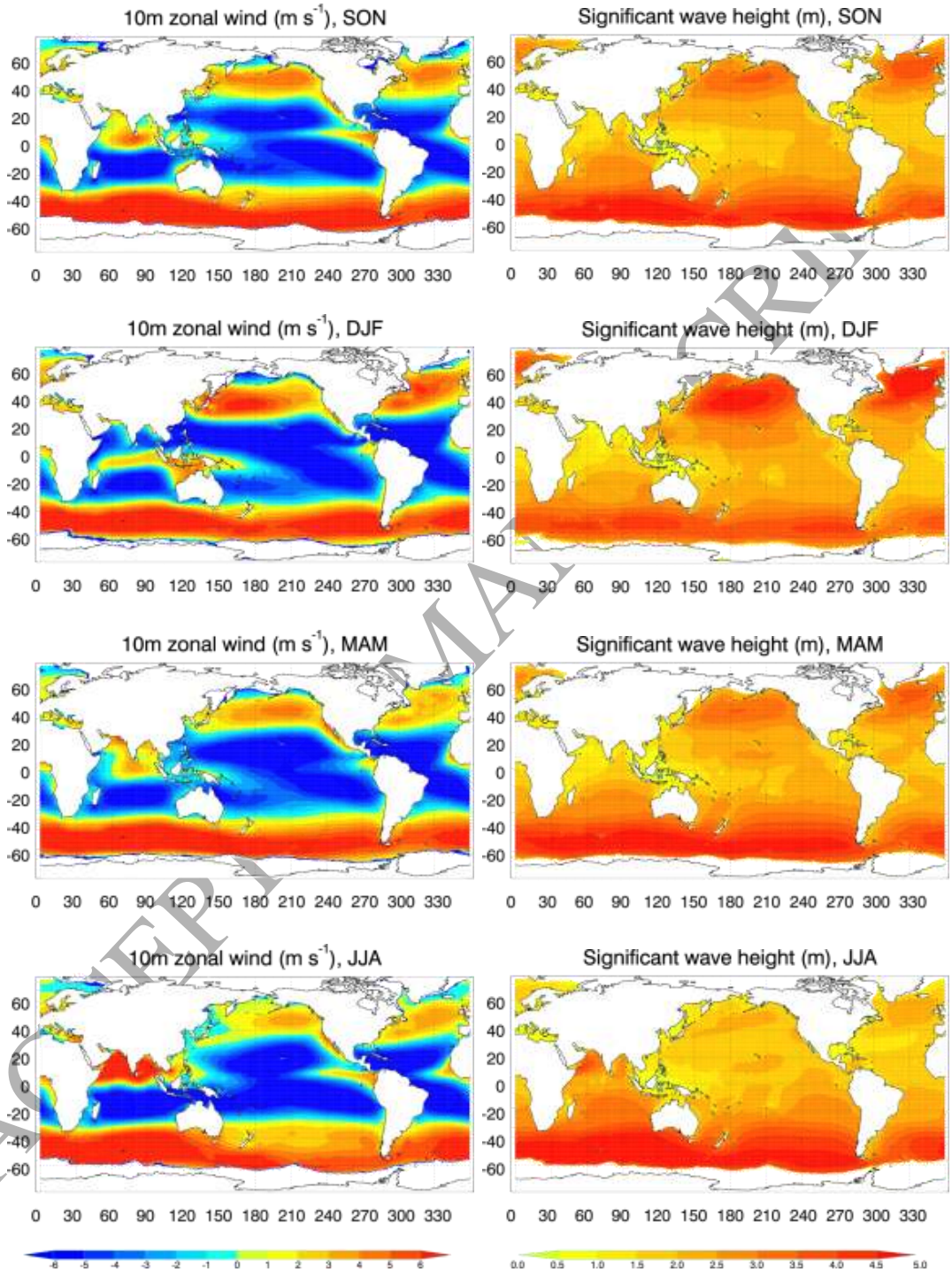

Figure 1: Mean fields for 10m zonal wind (left) and H_s (right), for each season over the period 1979-2009.

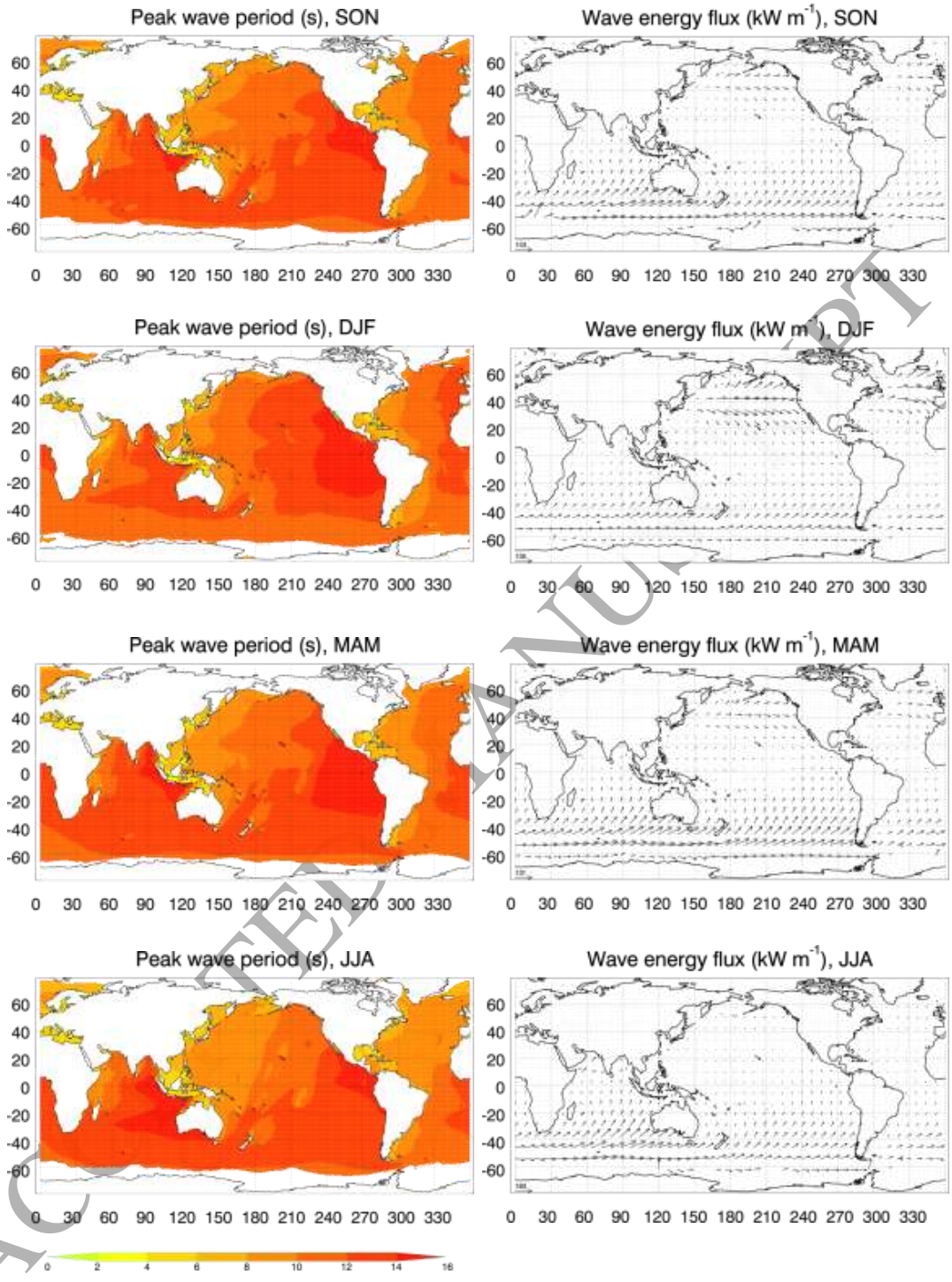

Figure 2: Same as Figure 1 but for T_p (left) and C_gE (right). C_gE means are calculated using zonal and meridional vector components; the magnitude of the longest vector is indicated in the lower left corner of the figure panel.

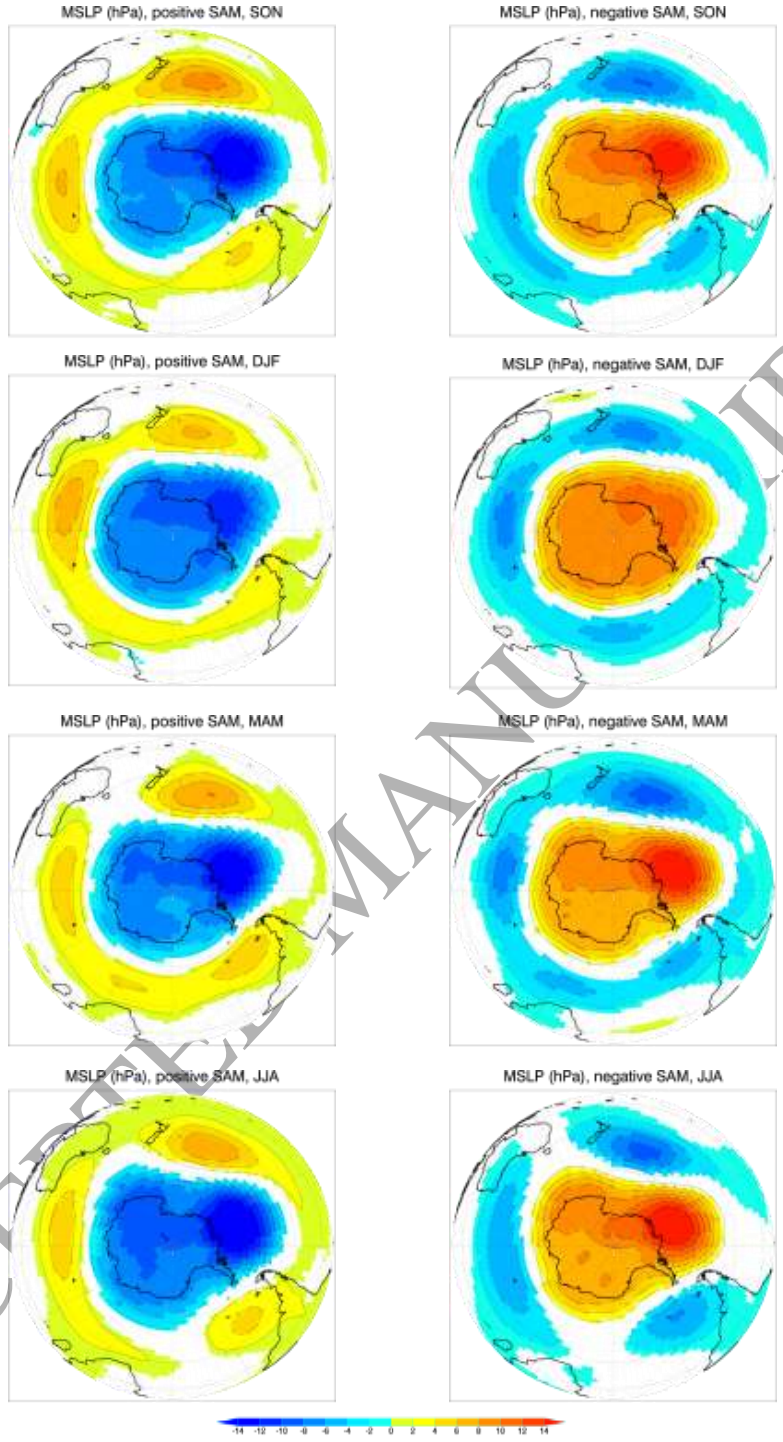

Figure 3: Composite MSLP anomalies (hPa) for positive (left column) and negative (right column) phases of the SAM, for each season over the period 1979-2009. Statistically significant anomalies are shaded (95% confidence using Student's t-test).

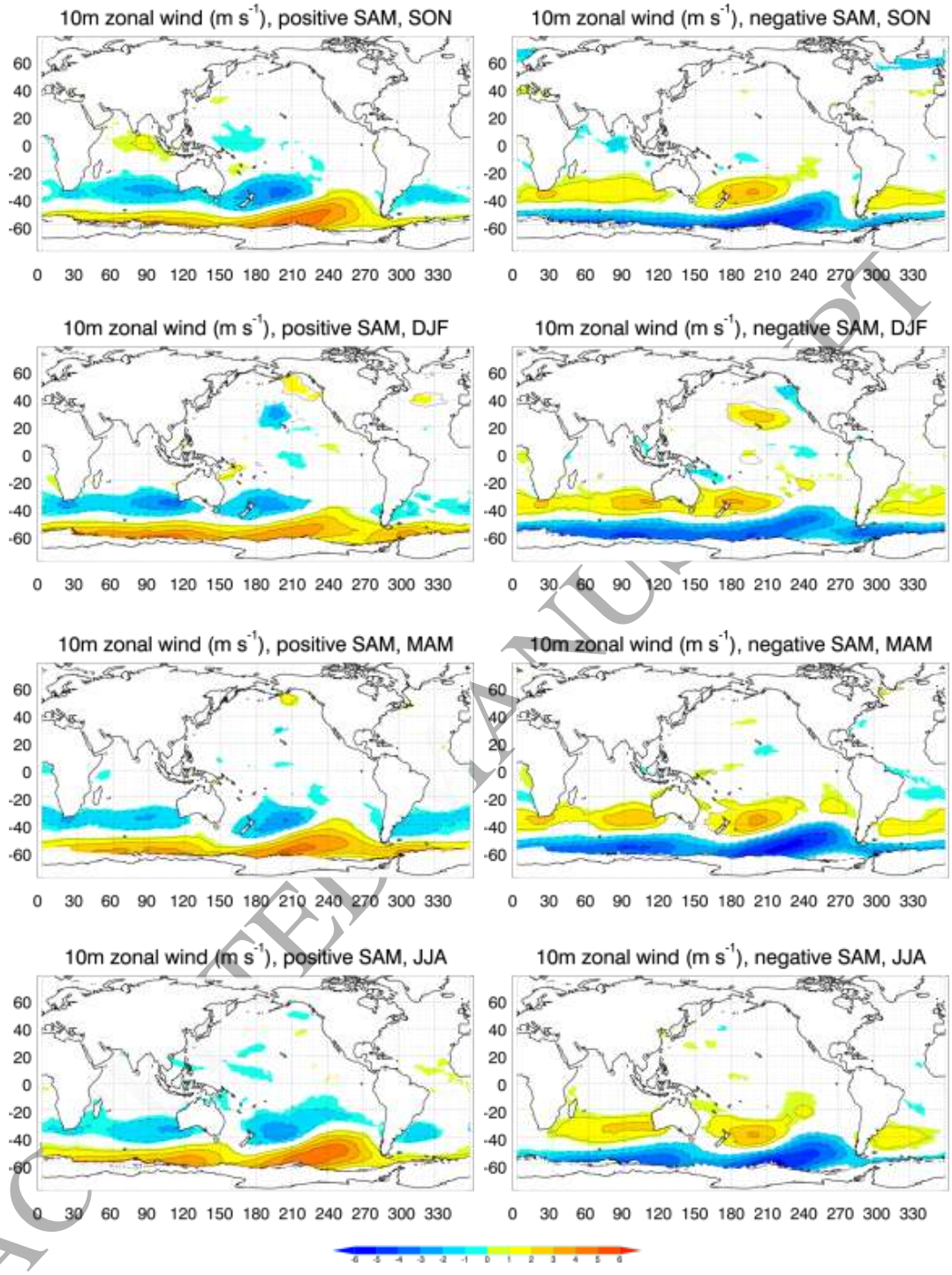

Figure 4: Same as Figure 3 but for 10m zonal wind anomalies (m s^{-1}).

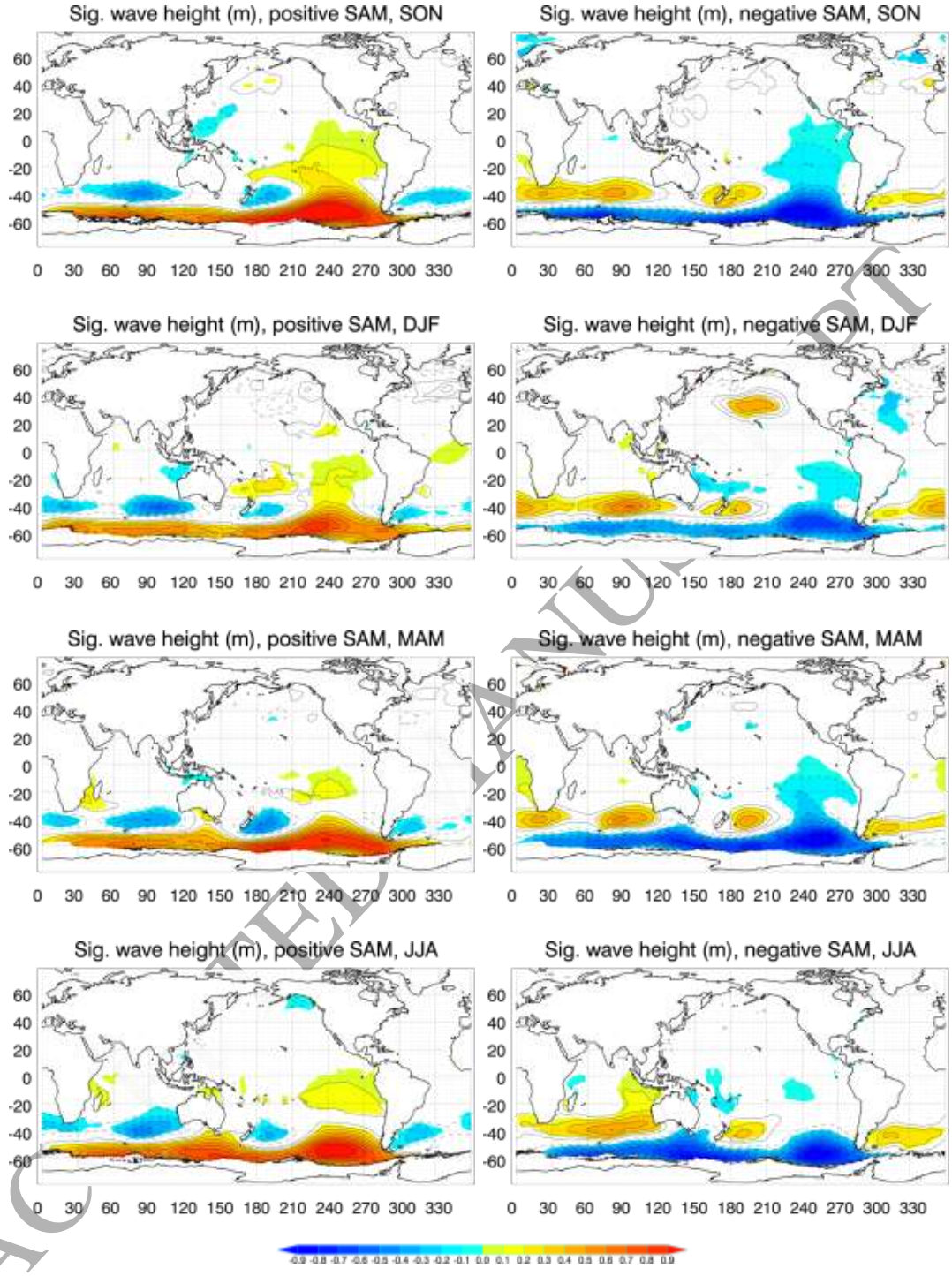

Figure 5: Same as Figure 3 but for H_s anomalies (m).

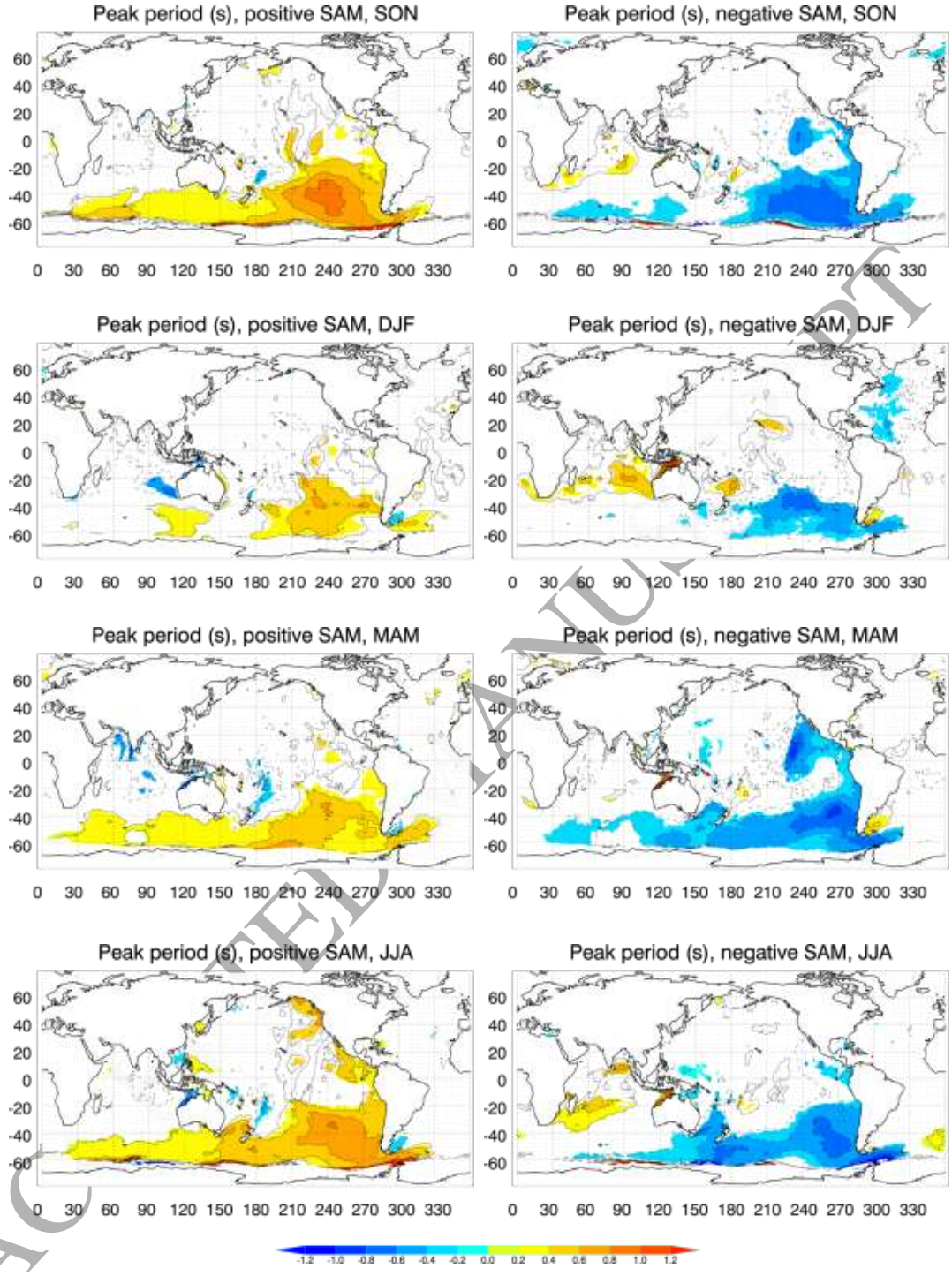

Figure 6: Same as Figure 3 but for T_p anomalies (s).

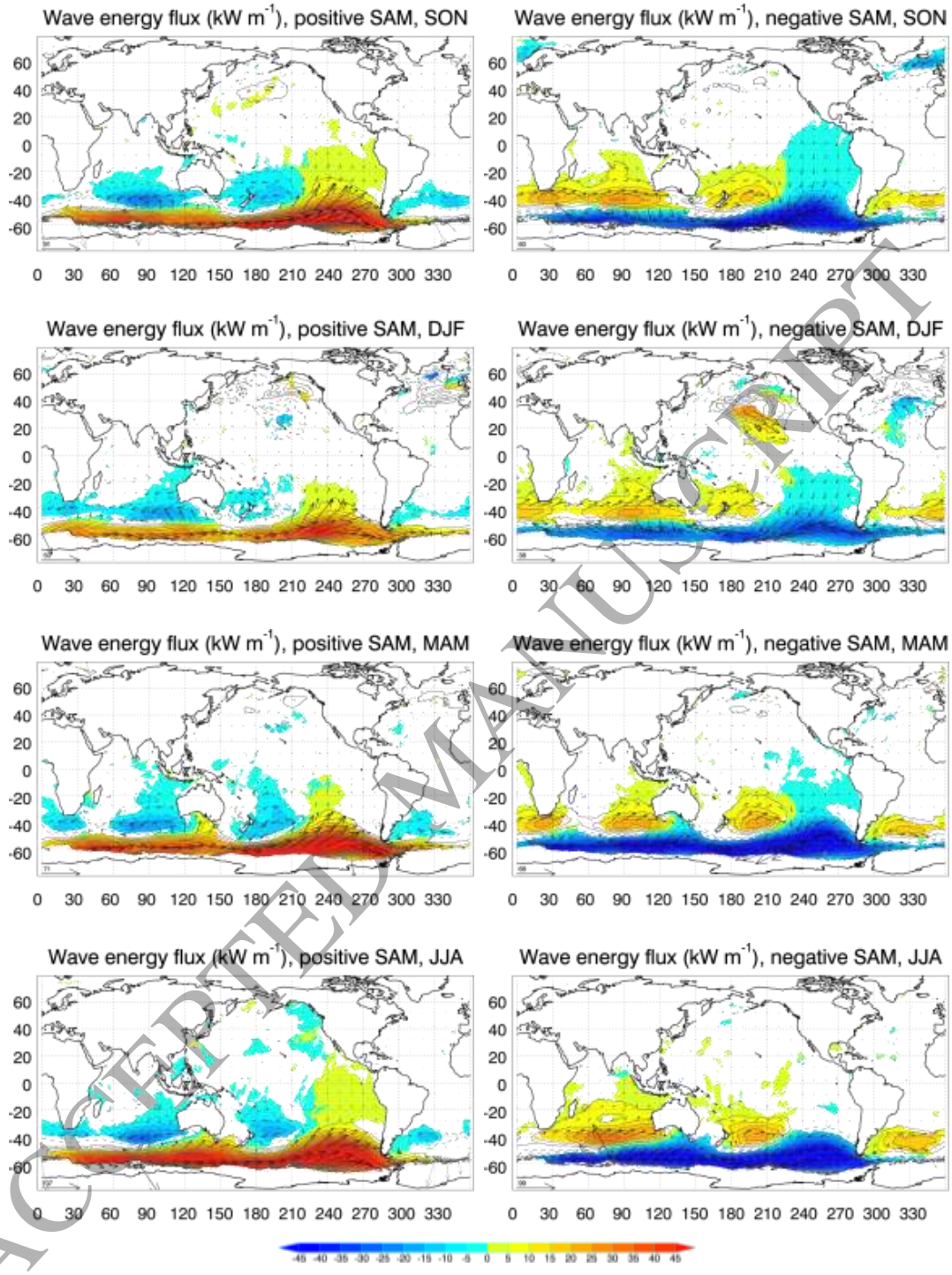

Figure 7: Same as Figure 3 but for zonal C_gE anomalies (kW m^{-1}). Superimposed over the significant shaded anomalies are C_gE vectors (comprising the zonal and meridional components), with the magnitude of the largest vector indicated in the lower left corner of each panel.

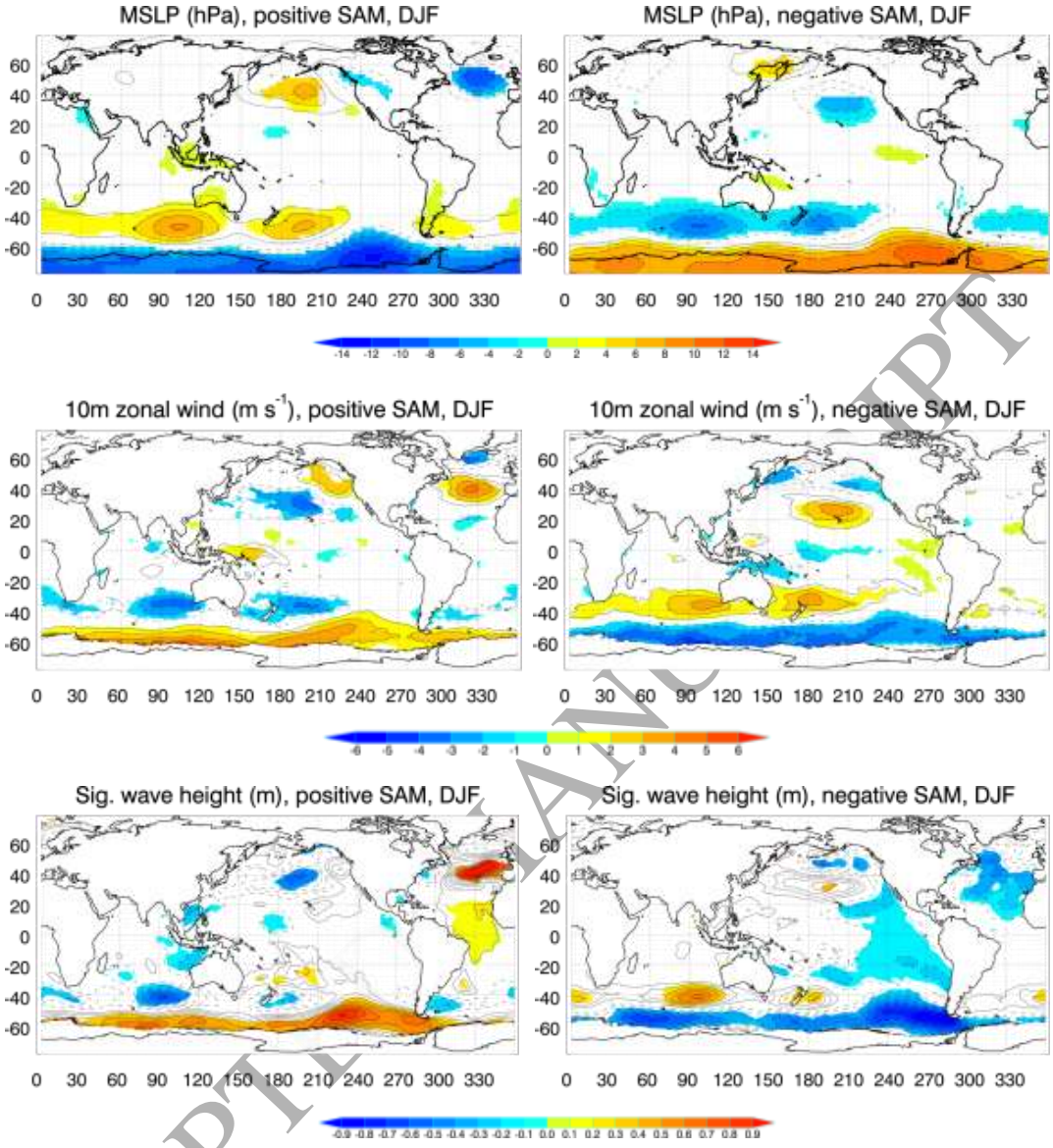

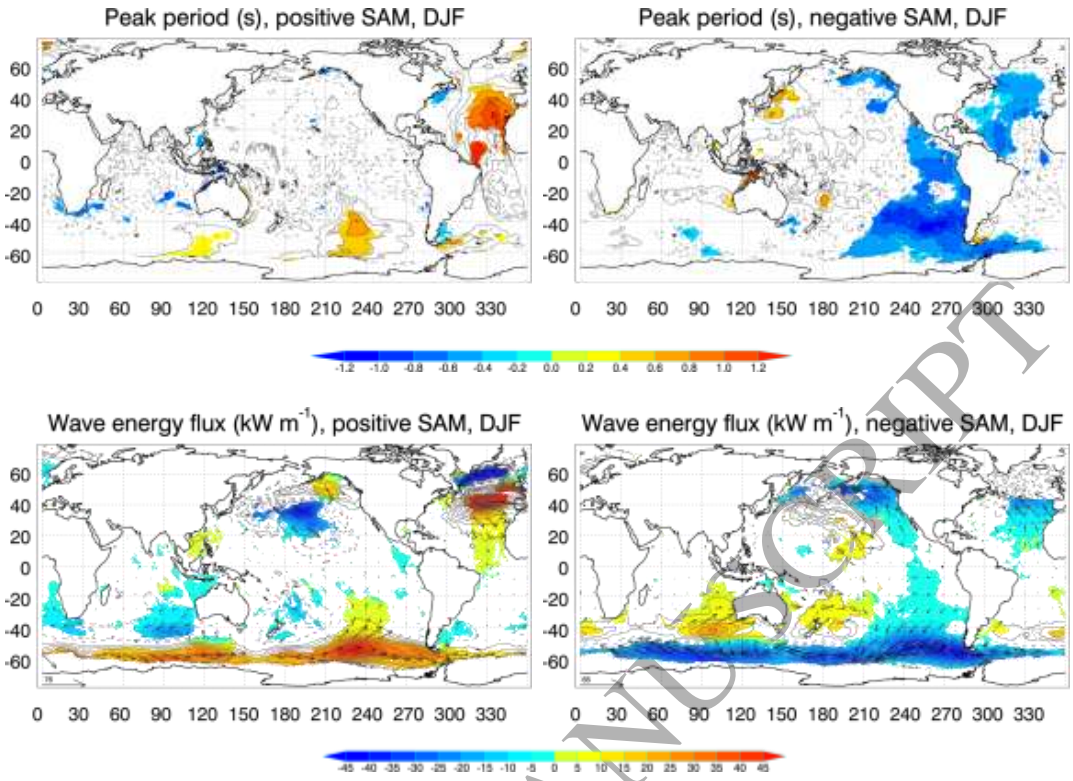

Figure 8: Composite anomalies in MSLP (hPa), 10m zonal wind (m s^{-1}), H_s (m), T_p (s) and C_gE (kW m^{-1}) for positive (left column) and negative (right column) phases of the SAM, for DJF over the period 1979-2009, after excluding El Niño and La Niña episodes from the analysis. Statistically significant anomalies are shaded (95% confidence using Student's t-test).

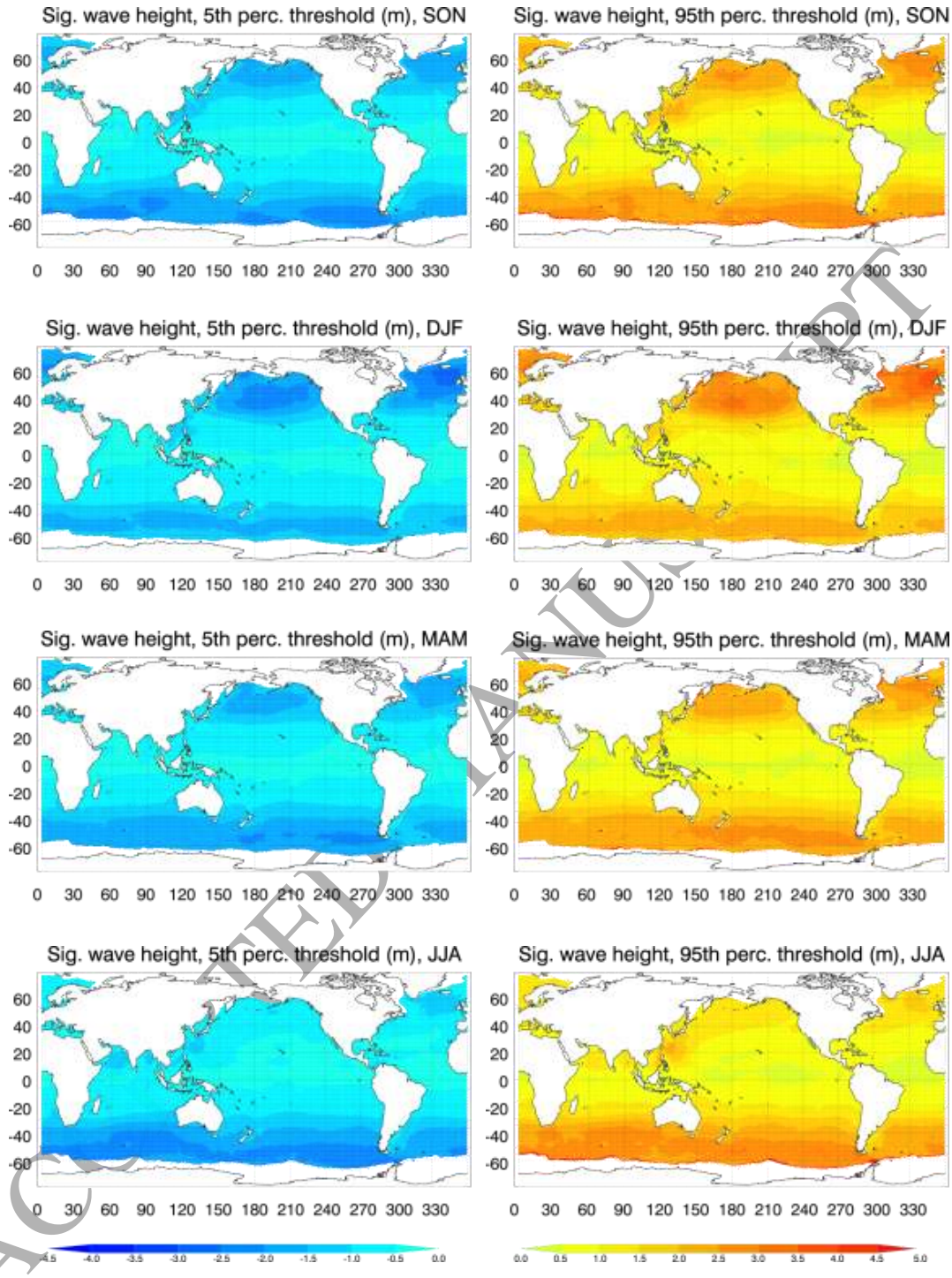

Figure 9: Threshold for H_s anomalies (m) below the 5th percentile (left column) and above the 95th percentile (right column), for each season over the period 1979-2009, displayed relative to mean Hs shown in Figure 1.

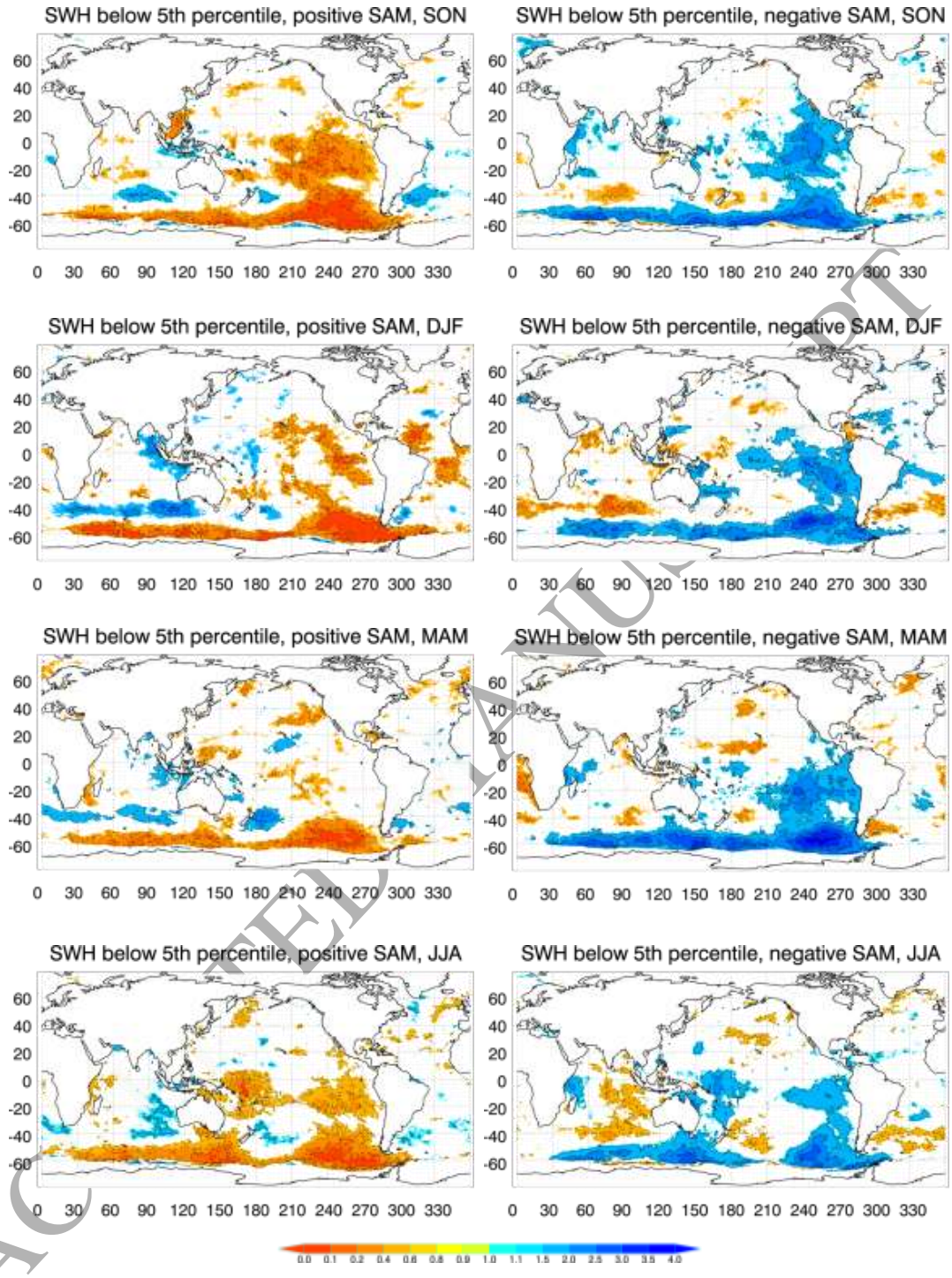

Figure 10: Ratio of probabilities of H_s anomalies below the 5th percentile for positive (left column) and negative (right column) phases of the SAM, for each season over the period 1979-2009. Ratios are calculated relative to the mean 5th percentile probability (nominally

0.05), and shading is applied where the ratio is significantly different from one at 95% confidence using a z-score test for event probabilities.

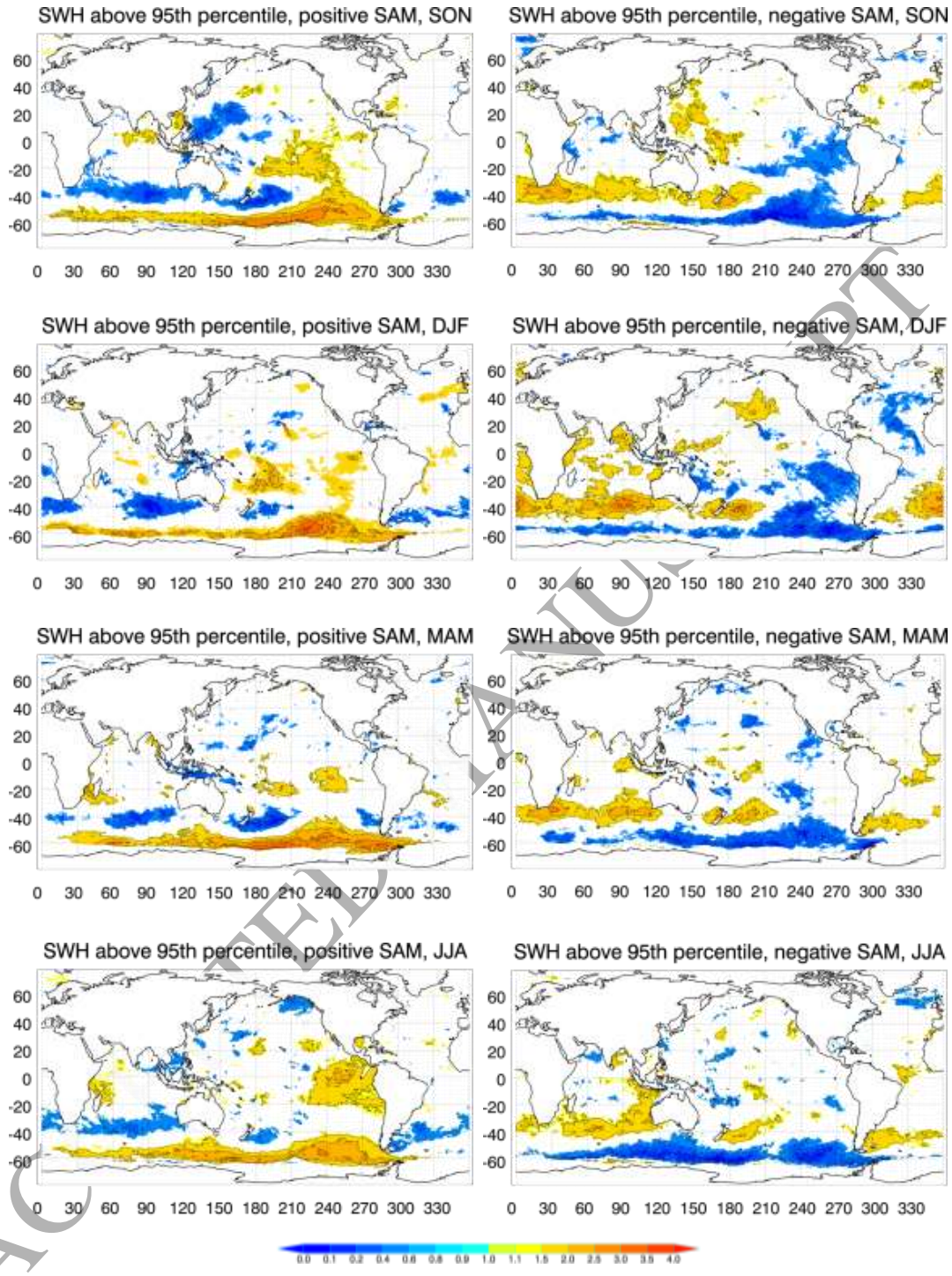

Figure 11: Same as Figure 10 except above the 95th percentile.

Table Caption

Table 1: Sample size *n* days and effective sample size n_{eff} days pertaining to each composite SAM phase (positive | negative) in each season, 1979-2009. Also shown in italics are the sample sizes for DJF when ENSO episodes are excluded from the analysis.

Season	MAM	JJA	SON	DJF
n	381 | 388	549 | 542	505 | 487	287 | 341
n (excluding ENSO)				*140 | 203*
$\mathbf{n_{eff}}$	114 | 81	113 | 107	96 | 88	82 | 61
$\boldsymbol{n_{eff}}$ ***(excluding ENSO)***				*40 | 41*